INT. J. REMOTE SENSING, 10 JANUARY, 2004,
VOL. 25, NO. 1, 15–37

Taylor & Francis
Taylor & Francis Group

# Analysis of Temperature Emissivity Separation (TES) algorithm applicability and sensitivity

V. PAYAN* and A. ROYER

Centre d'Applications et de Recherches en Télédétection, Université de Sherbrooke, Sherbrooke, J1K 2R1, Québec, Canada

**Abstract.** The purpose of this paper is to assess the spectral Temperature Emissivity Separation algorithm (TES) proposed by Gillespie *et al.* (1998) as a simple method to retrieve surface emissivity from ground-based measurements. First, we validate different empirical relationships for the Minimum Maximum Difference module, on which the TES is based, with a large dataset (about 500 surfaces from the Advanced Spaceborne Thermal Emission and Reflection Radiometer (ASTER) spectral library including man-made materials) for multiband data in the long wave infrared (LWIR: 7.5–14 $\mu$m), and hyperspectral data in the middle wave infrared (MWIR: 3.4–5.2 $\mu$m) and LWIR. We show the applicability of TES for hyperspectral data using a specific empirical relationship; this is confirmed by experimental measurements. For multiband data, we improve the TES for high contrast emissivity surfaces by integrating broadband 8–14 $\mu$m measurements in the iterative algorithm. We also found that metals do not confirm these empirical relationships. TES accuracy, extensively assessed by simulations, remains for multiband simulations (respectively for hyperspectral) within about 0.03 (0.02) for emissivity and within about 1.2 K (0.3 K) for temperature. However, surfaces with low maximum emissivity give higher errors. Except for these particular surfaces, the TES approach, applied on measurements from a portable multiband thermal radiometer, appears as the most efficient and accurate method for emissivity determination in the field without any *a priori* assumption on the surface nature.

## 1. Introduction

Heat transfer estimation and modelling at global scale are needed for understanding climate processes and relationships between soils and the environment. For climate and environmental studies, global monitoring of temperature is of particular interest.

For the range of Earth temperatures (except fires and volcanoes), maximum radiometric emission is found in the infrared spectral region, which contains two atmospheric windows: middle wave infrared (MWIR: 3.4–5.2 $\mu$m) and long wave infrared (LWIR: 7.5–14 $\mu$m, also referred to as thermal infrared). Moreover, radiance measurements made in these two windows allow emissivity estimation, which is a thermo-optical intrinsic property of the surface and of its physical state.

*Corresponding author; e-mail: vpayan@hermes.usherb.ca

*International Journal of Remote Sensing*
ISSN 0143-1161 print/ISSN 1366-5901 online 
http://www.tandf.co.uk/journals
DOI: 10.1080/0143116031000115274

Recent spaceborne thermal infrared multispectral sensors, such as the Advanced Spaceborne Thermal Emission and Reflection Radiometer (ASTER) sensor on the National Aeronautics and Space Administration (NASA)'s Earth Observing System TERRA satellite (Yamaguchi *et al.* 1998), are carrying out such measurements at local and global scale.

Decorrelation of emissivity and temperature from infrared measurements is not a trivial task. Since the surface is characterized by its temperature and by one emissivity for each spectral band, there always remain more unknowns than measurements. Inversion methods have to make assumptions to bypass this difficulty. Some of these methods are described in Becker and Li (1990, 1995), Hook *et al.* (1992), Sobrino *et al.* (1994), Wan and Li (1997), Li *et al.* (1999), Ma *et al.* (2000) and reviewed by Dash *et al.* (2002). In particular, the Temperature Emissivity Separation (TES) algorithm, developed for ASTER data by Gillespie *et al.* (1998), combines the iterative removal of atmospheric radiance and an empirical relationship allowing absolute emissivity recovery.

This paper presents a theoretical study of the TES algorithm adapted for a multiband radiometer operating in LWIR and for a hyperspectral spectroradiometer operating in LWIR and MWIR in order to characterize surfaces from ground-based field measurements.

First, we recall some fundamental points of theory, we briefly describe the adapted TES algorithm flowchart and we detail our methodology for the simulations. Then we compare different empirical relationships and we analyse the TES algorithm sensitivity with numerical simulations for both multiband and hyperspectral approaches. Next, we propose improvements to overcome limitations of the original TES algorithm. Finally, we present some experimental results obtained with a multiband radiometer (CIMEL 312-2) and with a hyperspectral Fourier transform infrared (FTIR) spectroradiometer in emission (BOMEM MB100) to illustrate the applicability of the TES algorithm.

## 2. Theory and methodology

### 2.1. *At-sensor radiance and approximations on atmosphere*

The general form of the spectral radiance sensed by a radiometer in the direction $(\theta_r, \varphi_r)$ is:

$$L_\lambda(\theta_r,\varphi_r)=\left(\begin{array}{l}\varepsilon_\lambda(\theta_r,\varphi_r)B_\lambda(T_s)+\\ \int_{ih}\rho_{b,\lambda}(\theta_i,\varphi_i,\theta_r,\varphi_r)L_{atm\downarrow,\lambda}(\theta_i,\varphi_i)\cos\theta_i\,\mathrm{d}\omega_i+\\ \rho_{b,\lambda}(\theta_s,\varphi_s,\theta_r,\varphi_r)E_{sun,\lambda}(\theta_s)\end{array}\right)\tau_{atm\uparrow,\lambda}(\theta_r,\varphi_r)+L_{atm\uparrow,\lambda}(\theta_r,\varphi_r)\quad(1)$$

$B_\lambda(T_s)$ is the spectral radiance emitted by a blackbody at the surface temperature $T_s$, calculated with Planck's law. The surface emitted radiance is obtained by multiplying the blackbody radiance by $\varepsilon_\lambda(\theta_r, \varphi_r)$, the spectral directional emissivity. $\rho_{b,\lambda}(\theta_i,\varphi_i,\theta_r,\varphi_r)$ is the bidirectional spectral reflectance (in $\mathrm{sr}^{-1}$) corresponding to the bidirectional reflectance distribution function (BRDF) from Nicodemus *et al.* (1977). $L_{atm\downarrow,\lambda}(\theta_i,\varphi_i)$ is the downwelling radiance emitted and diffused by the atmosphere. To obtain the global contribution of the atmosphere, one must integrate $\rho_{b,\lambda}(\theta_i,\varphi_i,\theta_r,\varphi_r)$ and $L_{atm\downarrow,\lambda}(\theta_i,\varphi_i)$ over the incident hemisphere (noted *ih*). $E_{sun,\lambda}(\theta_s)=\tau_{atm\downarrow,\lambda}(\theta_s)E_{o,\lambda}\cos\theta_s$ is the direct solar irradiance at ground level, with $E_{o,\lambda}$ the direct solar irradiance at the top of atmosphere, $\theta_s$ the zenithal solar

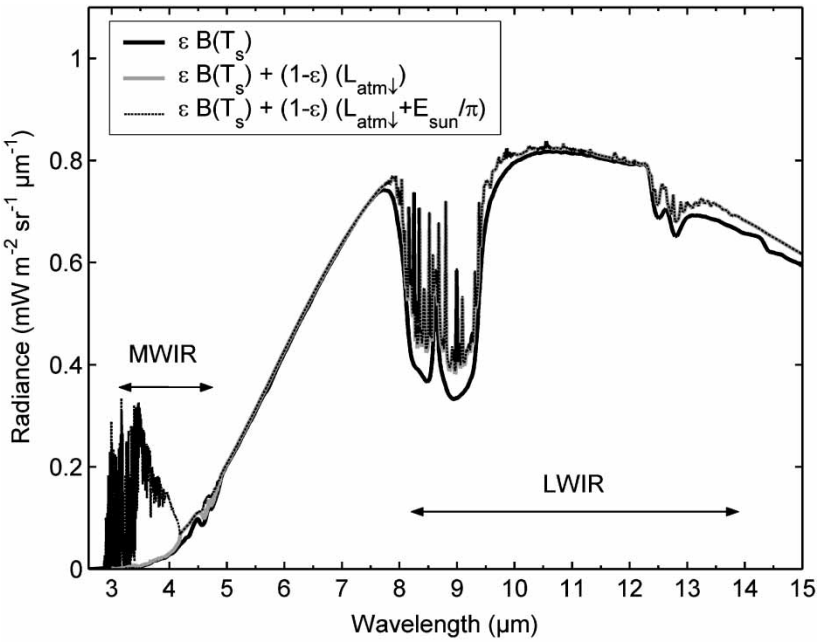


Figure 1. Ground-level radiance simulations for surface emitted signal and at-sensor signal. The simulation parameters are as follows: MODTRAN 4.0 radiative transfer code; 1976 US Standard model atmosphere; solar zenith angle = 45°; $SiO_2$ emissivity spectrum; $T_s = 20°C$.

angle and $\tau_{atm\downarrow,\lambda}(\theta_s)$ the total atmosphere transmittance. To obtain the reflected solar radiance in the direction ($\theta_r$, $\varphi_r$), $E_{sun,\lambda}(\theta_s)$ is multiplied by $\rho_{b,\lambda}(\theta_s, \varphi_s, \theta_r, \varphi_r)$. The direct solar irradiance is negligible in LWIR but is significant in MWIR as illustrated in figure 1. It should be noted that we do not take into account the diffuse solar irradiance. Indeed molecular scattering in the atmosphere is practically non-existent in the thermal infrared, and the scattering due to aerosols can be reasonably neglected in this domain for a small quantity of aerosols. $\tau_{atm\uparrow,\lambda}(\theta_r, \varphi_r)$ is the atmospheric transmittance between the surface and the radiometer. $L_{atm\uparrow,\lambda}(\theta_r, \varphi_r)$ is the radiance directly emitted by the atmosphere layer toward the sensor. If we consider measurements at ground level, the influence of the atmosphere between the surface and the sensor can be neglected (error less than 0.02% in LWIR and about 2% in MWIR, based on MODTRAN simulations). Moreover, if the incident atmospheric radiance is isotropic (Norman and Becker 1995; approximation valid for angles between 0° and 60°) it can be removed from the integral. Then the bidirectional reflectance integrated over the incident hemisphere can be considered as a hemispherical–directional reflectance $\rho_{hd,\lambda}$ (Norman and Becker 1995). This hemispherical–directional reflectance is related to the directional emissivity by Kirchhoff's law $\left(\rho_{hd,\lambda}(\theta_r, \varphi_r) = 1 - \varepsilon_\lambda(\theta_r, \varphi_r)\right)$, the applicability of which was verified on natural surfaces by numerous authors for both laboratory and field conditions (Salisbury *et al.* 1994, Ninomiya *et al.* 1997, Korb *et al.* 1999). Therefore the second term in equation (1)

becomes:

$$\begin{aligned}
&\int_{ih} \rho_{b,\lambda}(\theta_i, \varphi_i, \theta_r, \varphi_r) L_{atm\downarrow,\lambda}(\theta_i, \varphi_i) cos\theta_i \, \mathrm{d}\omega_i \\
&= L_{atm\downarrow,\lambda} \int_{ih} \rho_{b,\lambda}(\theta_i, \varphi_i, \theta_r, \varphi_r) \cos\theta_i \, \mathrm{d}\omega_i \\
&= \rho_{hd,\lambda}(\theta_r, \varphi_r) L_{atm\downarrow,\lambda} \\
&= (1 - \varepsilon_\lambda(\theta_r, \varphi_r)) L_{atm\downarrow,\lambda}
\end{aligned} \tag{2}$$

Finally, equation (1) can be rewritten at ground level as:

$$L_\lambda(\theta_r, \varphi_r) = \varepsilon_\lambda(\theta_r, \varphi_r) B_\lambda(T_s) + (1 - \varepsilon_\lambda(\theta_r, \varphi_r)) L_{atm\downarrow,\lambda} + \rho_{b,\lambda}(\theta_s, \varphi_s, \theta_r, \varphi_r) E_{sun,\lambda}(\theta_s) \tag{3}$$

Considering a discrete band radiometer, equation (3) must be integrated over the instrument spectral response ($f_\lambda$). The at-sensor radiance for the band $j$ is then defined as:

$$\begin{aligned}
L_j(\theta_r, \varphi_r) &= \int f_\lambda L_\lambda(\theta_r, \varphi_r) \mathrm{d}\lambda \\
&= \int f_\lambda \varepsilon_\lambda(\theta_r, \varphi_r) B_\lambda(T_s) \mathrm{d}\lambda + \int f_\lambda (1 - \varepsilon_\lambda(\theta_r, \varphi_r)) L_{atm\downarrow,\lambda} \, \mathrm{d}\lambda \\
&\quad + \int f_\lambda \rho_{b,\lambda}(\theta_s, \varphi_s, \theta_r, \varphi_r) E_{sun,\lambda}(\theta_s) \mathrm{d}\lambda
\end{aligned} \tag{4}$$

Note that in our theoretical simulations, $f_\lambda$ is not normalized, taking into account the instrument response amplitude.

But estimating a band emissivity from equation (4) is not easy. This equation cannot be solved, as bidirectional reflectance is generally unknown and the spectral expressions for emissivity and radiances are coupled inside the integrals.

To bypass the difficulties arising from equation (4), we use an approximated expression commonly used in thermal infrared remote sensing for measured at-sensor radiance (Becker and Li 1995):

$$L_{sens,j}(\theta_r, \varphi_r) = \varepsilon_j(\theta_r, \varphi_r) B_j(T_s) + \big(1 - \varepsilon_j(\theta_r, \varphi_r)\big) L_{atm\downarrow,j} + \rho_{b,j}(\theta_s, \varphi_s, \theta_r, \varphi_r) E_{sun,j}(\theta_s) \tag{5}$$

It should be noted that equation (5) is not a mathematical equivalent to equation (4), but this could be justified if the surface spectral behaviour is reasonably constant in the bands considered (Malaplate 2001).

In equation (5), $B_j$, $L_{atm\downarrow,j}$ and $E_{sun,j}$ are defined as $X_j = \int f_\lambda X_\lambda \, \mathrm{d}\lambda$.

The bidirectional reflectance for a band $j$ can be defined as a weighted average given by:

$$\rho_{b,j}(\theta_s, \varphi_s, \theta_r, \varphi_r) = \frac{\int f_\lambda \rho_{b,\lambda}(\theta_s, \varphi_s, \theta_r, \varphi_r) \mathrm{d}\lambda}{\int f_\lambda \, \mathrm{d}\lambda} \tag{6}$$

and then has to be measured independently. In the special case where the surface can be considered as Lambertian, bidirectional reflectance is related to

hemispherical–directional reflectance by $\pi\rho_b = \rho_{hd}$, and then to emissivity according to Kirchhoff's law.

Band emissivity $\varepsilon_j$ can be defined as a band average emissivity as in equation (7) or, as in the case of the spectral emissivity definition, as the ratio between the surface emitted radiance to the blackbody radiance at the same temperature as in equation (8).

$$\varepsilon_j(\theta_r, \varphi_r) = \frac{\int f_\lambda \varepsilon_\lambda(\theta_r, \varphi_r)\mathrm{d}\lambda}{\int f_\lambda \,\mathrm{d}\lambda} \tag{7}$$

$$<\varepsilon_j(\theta_r, \varphi_r)> = \frac{\int f_\lambda \varepsilon_\lambda(\theta_r, \varphi_r) B_\lambda(T_s)\mathrm{d}\lambda}{\int f_\lambda B_\lambda(T_s)\mathrm{d}\lambda} \tag{8}$$

But equation (8) is temperature dependent especially if the emissivity spectrum presents strong variations in the wavelength interval considered (Staaf *et al.* 1996). Equation (7) is preferred, as it is temperature independent as recommended by Becker and Li (1990). Defined as in equation (7), band emissivity $\varepsilon_j$ is an intrinsic property of the surface.

## 2.2. *TES algorithm*

The TES algorithm was developed by Gillespie *et al.* (1998) for the five LWIR bands of the ASTER imaging radiometer. The TES algorithm combines three algorithms linked together as shown in figure 2 and is valid for multiband and hyperspectral data. The three modules are:

- the Normalized Emissivity Method (NEM), which removes environmental radiance and gives a first guess of temperature and emissivities assuming a maximum value for emissivities;
- the Ratio module (Watson 1992) where NEM emissivities are ratioed to their average (equation (9))
- the Minimum Maximum Difference (MMD, equation (10)) module that allows absolute emissivity retrieval using an empirical relationship to predict $\varepsilon_{\min}$ (equation (11)).

$$\beta_{j \text{ or } \lambda} = \frac{\varepsilon_{j \text{ or } \lambda}}{\dfrac{1}{k}\displaystyle\sum_{j \text{ or } \lambda=1}^{k} \varepsilon_{j \text{ or } \lambda}} \tag{9}$$

$$MMD = \max\left(\beta_{j \text{ or } \lambda}\right) - \min\left(\beta_{j \text{ or } \lambda}\right) \tag{10}$$

$$\varepsilon_{\min} = r + s \times MMD^t \tag{11}$$

with $r = 0.994$, $s = -0.687$, $t = 0.737$ for ASTER bands (Gillespie *et al.* 1998), $j$ refers to a band, $\lambda$ to a wavelength and $k$ is the number of bands. Each emissivity is then estimated with:

$$\varepsilon_{j \text{ or } \lambda} = \beta_{j \text{ or } \lambda} \frac{\varepsilon_{\min}}{\min\left(\beta_{j \text{ or } \lambda}\right)} \tag{12}$$

Another empirical relationship was proposed by Gu and Gillespie (2000). This relation, referred to here as the Minimum Maximum Ratio (MMR) relation, is

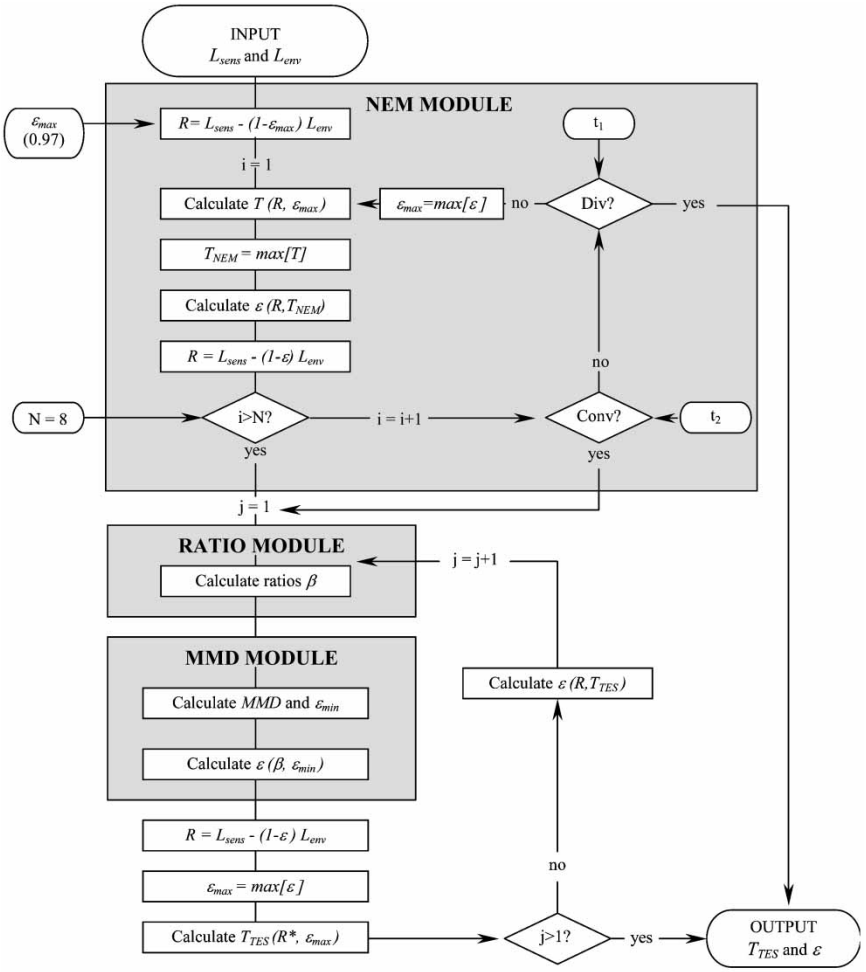


Figure 2. Flow diagram of the TES algorithm. $R$, $\varepsilon$, $L_{sens}$, $L_{env}$, $T$ and $\beta$ are vectors with as many elements as sensor bands (hyperspectral or multispectral). $R^*$ is the radiance for the maximum emissivity band.

defined as:

$$\ln \varepsilon_{\min} = m \ln(MMR) + p \tag{13}$$

with $MMR = \varepsilon_{\min}/\varepsilon_{\max}$ and $m = 1.056$, $p = -0.01$ for ASTER bands. These coefficients and those of equation (11) were established for ASTER channels, using about 100 natural surface spectra of the ASTER spectral library (http://speclib.jpl.nasa.gov/).

## 2.3. *Emissivity dataset*

Reference spectral data used in this study were taken from the ASTER spectral library (V1.2, available on CD-ROM or on-line at http://speclib.jpl.nasa.gov/). This spectral library is made up of three other spectral libraries: the Jet Propulsion Laboratory (JPL), the Johns Hopkins University (JHU), and the United States Geological Survey (USGS—Reston) Spectral Libraries. It contains reflectance

spectra acquired from the visible to the mid-infrared range of soils, minerals, vegetation, water and man-made materials. From the ASTER spectral library, we selected about 500 directional–hemispherical reflectance spectra containing data in MWIR and LWIR (excluding bidirectional reflectivity measurements, meteorite and lunar materials).

Individual emissivity spectra were deducted from Kirchhoff's law. The spectra of fine powdered samples (particle size $<75\,\mu$m for JHU library and $<45\,\mu$m for JPL library, plus samples identified as clay) were eliminated because they may not follow this law (Salisbury *et al.* 1994, Korb *et al.* 1999). About 10 other spectra were also excluded.

In the case of the hyperspectral study, we interpolated emissivity spectra at a constant wavenumber interval of $2\,\mathrm{cm}^{-1}$ to simulate our spectroradiometer response (FTIR BOMEM MB100). Data outside the LWIR and MWIR atmospheric windows were not considered, as well as the data from the $CO_2$ absorption band (4.2–4.5 $\mu$m).

In the case of the multiband study, all the spectra considered were interpolated to a constant wavenumber interval of $5\,\mathrm{cm}^{-1}$ to match the spectral response $f$ of our multiband radiometer. This radiometer (CIMEL 312-2) has five bands in LWIR, which are very similar to ASTER bands, plus one broad band as presented in figure 3. Then the spectra were integrated numerically:

$$\varepsilon_j = \frac{\int f_\sigma \varepsilon_\sigma \,\mathrm{d}\sigma}{\int f_\sigma \,\mathrm{d}\sigma} \approx \frac{\sum_k f(\sigma_k)\varepsilon(\sigma_k)(\sigma_k - \sigma_{k+1})}{\sum_k f(\sigma_k)(\sigma_k - \sigma_{k+1})} \tag{14}$$

where $\sigma$ stands for the wavenumber.

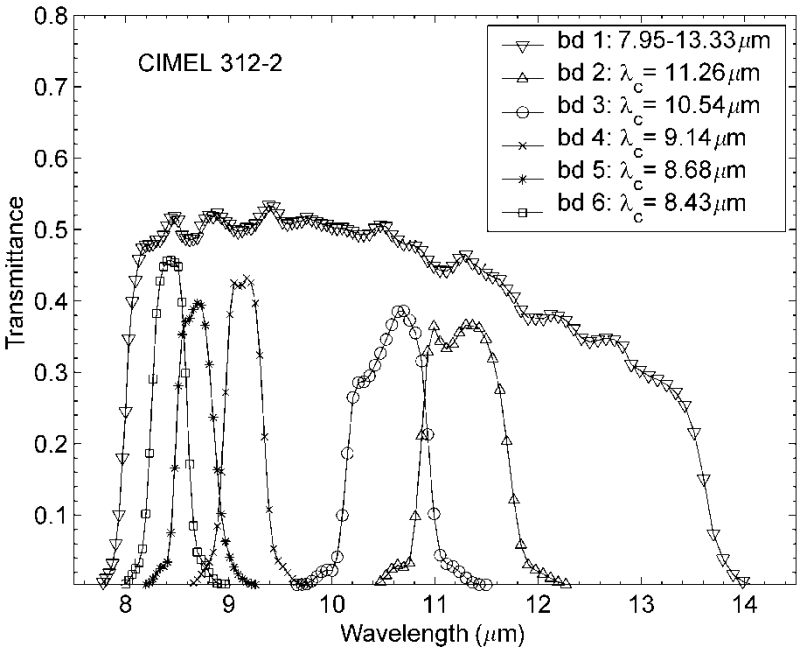


Figure 3. Spectral response of the portable CIMEL 312-2 radiometer used for simulation and measurements. $\lambda_c$ is the central wavelength of each band.

In order to recompute the equations relating $\varepsilon_{\min}$ to the contrast (e.g. MMD or MMR), we used a least-squares optimization technique in both multiband and hyperspectral cases.

### 2.4. *Simulated inputs for the TES algorithm*

To run the TES algorithm, both environment radiation and at-sensor radiance have to be supplied as input parameters to the model (figure 2).

First of all, let us consider environment radiation. In the general form, it includes the direct solar irradiance, the downwelling atmospheric radiance and the radiance from surrounding objects. For the present simulation we neglected the last term. The direct solar irradiance was simulated using MODTRAN 4.0 for a zenithal solar angle of 45° in summer. The atmosphere was modelled using the 1976 US standard model atmosphere from sea level and in a clear sky condition. Concerning the downwelling atmospheric radiance $L_{atm\downarrow,\lambda}$, we supposed earlier (equation (2)) that it is isotropic, i.e. independent of angles. In equation (15), we estimated its average value by dividing the thermal flux density from the complete hemisphere (noted $F_{sky,\lambda}$) by $\pi$, the solid angle corresponding to this hemisphere. Moreover, one can numerically prove that this radiance can be estimated with a 1.1% accuracy by the numeric value of the downwelling atmospheric radiance measured at 53°, for the 1976 US standard model atmosphere of MODTRAN 4.0. The value of this angle can be refined when using another atmosphere model or other water equivalent amount. A similar calculation was carried out by Otterman *et al.* (1994) to connect the directional and hemispherical apparent temperatures of a vegetated terrain.

$$L_{atm\downarrow,\lambda} = \frac{F_{sky,\lambda}}{\pi} \approx L_{atm\downarrow,\lambda}(53^\circ) \tag{15}$$

The second input for the TES algorithm is at-sensor radiance. In the hyperspectral case, it is defined as in equation (3) in which we replace $\rho_b$ by $(1-\varepsilon)/\pi$ by assuming that surfaces are Lambertian. In the LWIR region, where direct sun irradiance can be neglected, or for simulated measurements of shaded surfaces (direct Sun irradiance removed), this assumption is not necessary. In the case of multiband simulations, the discrete values of all the spectral radiances $L_{x,\lambda}$ were integrated numerically over the spectral response $f_\lambda$ of our multiband radiometer to compute the radiance $L_{x,j}$ at a band $j$:

$$L_{x,j} = \int f_\lambda L_{x,\lambda}\, \mathrm{d}\lambda \approx \sum_k f(\lambda_k) L_x(\lambda_k)(\lambda_k - \lambda_{k+1}) \tag{16}$$

Thus the at-sensor radiance for the band $j$ in the LWIR region is:

$$L_{sens,j} = \varepsilon_j B_j(T_s) + (1-\varepsilon_j) L_{atm\downarrow,j} \tag{17}$$

where $\varepsilon_j$ is the emissivity corresponding to the band $j$ calculated using equation (7). $B_j(T_s)$ is the integrated blackbody radiance over the spectral band considered. It is evaluated using an approximated Planck function:

$$B_j(T_s) = \int f_\lambda B_\lambda(T_s)\mathrm{d}\lambda \approx a_j e^{-b_j/T_s^{n_j}} \tag{18}$$

$a_j$, $b_j$, $n_j$ are coefficients specific to the sensor spectral response. The coefficients used

here were computed for the CIMEL CE 312-2 radiometer to fit a radiance expressed in mW $cm^{-2} sr^{-1}$, with $T$ in K.

In all simulations the surface temperature is set at 20°C.

## 3. Results

### 3.1. *Analysis of empirical MMD and MMR relationships*

Empirical relations in the form of MMD (equation (11)) and MMR (equation (13)) are derived and compared to the original relations. This comparison is achieved both for multiband data in LWIR and for hyperspectral data in MWIR and in LWIR.

#### 3.1.1. *LWIR multiband analysis*

MMD fit based on 522 emissivity spectra resampled to the CIMEL 312-2 radiometer spectral bands is shown on figure 4. We found that equation (11) gives the best overall fit. The original coefficients are adapted for our five CIMEL bands, since they are very similar to ASTER bands. Of course, optimized equations would have to be computed if other spectral responses were considered.

Meanwhile, emissivity spectra with low maximum cause difficulties. As $\varepsilon_{max}$ decreases, observations move away from the MMD relation, as illustrated on figure 4 where points characterized by $\varepsilon_{max} < 0.9$ are identified. These surfaces correspond to different minerals such as carbonates, inosilicates, sulphates and oxides (ferrite, pewter oxide) with no other common characteristic.

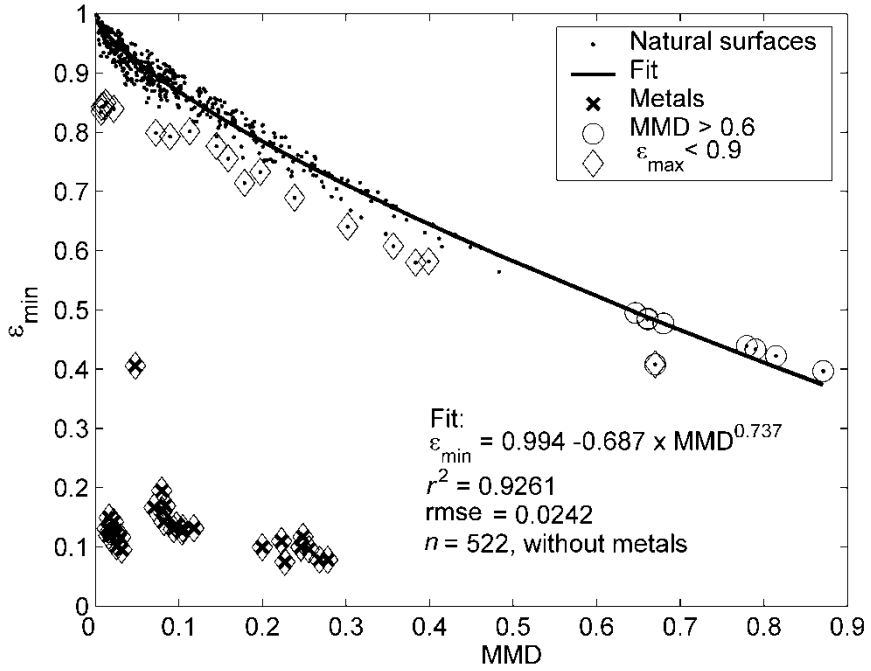


Figure 4. MMD relationship given by Gillespie *et al.* (1998) was assessed on 521 spectra from JPL, JHU and USGS libraries, including soils, minerals, vegetation, water and man-made materials but without metals (**x**). Two other sets were identified: surfaces with low maximum emissivity (diamonds) and surfaces with high contrast (circles); they are included in the regression.

The MMR relationship (equation (13)) was evaluated (not shown here) but we did not register improvements for the dataset considered. It should be noted that a linear relationship between MMD values and emissivity minimum values could also be considered, particularly if one does not take into account the spectra with low maximum or those with high contrast (respectively identified by diamonds and circles on figure 4). The relation is then significant but leads to a slight increase of rms error (rmse) (+10%) compared to a power law relationship like that of equation (11).

3.1.2. *MWIR and LWIR hyperspectral analysis*

The use of the MMD relationship (equation (11) or a linear form) with hyperspectral data is not appropriate in MWIR as these equations diverge when contrast increases, predicting negative emissivities for MMD > 1.6 (not shown here). Since emissivity contrasts are generally strong in MWIR, the MMR approach was preferred for hyperspectral data. Fits for LWIR, MWIR and MWIR + LWIR regions are plotted on figure 5(*a*), (*b*) and (*c*). For LWIR (figure 5(*a*)) and MWIR + LWIR (figure 5(*c*)), an MMR relation is well suited to describe the spectral behaviour of the analysed spectra. On figure 5(*b*), where the fit for MWIR is plotted, we observe important scattering around the fitted relation. Therefore, emissivities retrieved in this spectral domain may still be biased. Nevertheless, if we consider data in MWIR and LWIR, the fact that an empirical relationship can be defined for hyperspectral data is a first step in the assessment of TES applicability to hyperspectral measurements.

3.1.3. *Metal surfaces*

We noticed that metals are badly modelled by the empirical relationships both for multispectral and hyperspectral data. This is illustrated on figure 4 for multispectral data where metals are identified. These samples have very low emissivities—therefore high reflectances—and they are not good candidates for emissivity retrieval methods that assume high maximum emissivity. An alternative approach is discussed in §4.3.

3.2. *Analysis of TES sensitivity*

In order to quantify the error on emissivity retrieval by the TES algorithm from multispectral data and hyperspectral data, we simulated the radiance as measured by the sensor at ground level and then compared the emissivity retrieved by the TES algorithm to the one used to derive the simulated radiance. For this purpose we used the emissivity dataset described in §2.3 extracted from the ASTER spectral library, from which metal spectra are removed.

3.2.1. *LWIR multiband analysis*

3.2.1.1. *Sensitivity of TES to* $\varepsilon_{max}$ *input*

The NEM module allows recovery of the emissivity spectrum shape; the absolute value is conditioned by the input $\varepsilon_{max}$. Statistically speaking as most

Figure 5. Minimum Maximum Ratio relationship computed for hyperspectral LWIR (*a*), MWIR (*b*) and MWIR–LWIR (*c*) emissivity spectra and compared to the one initially proposed by Gu and Gillespie (2000).

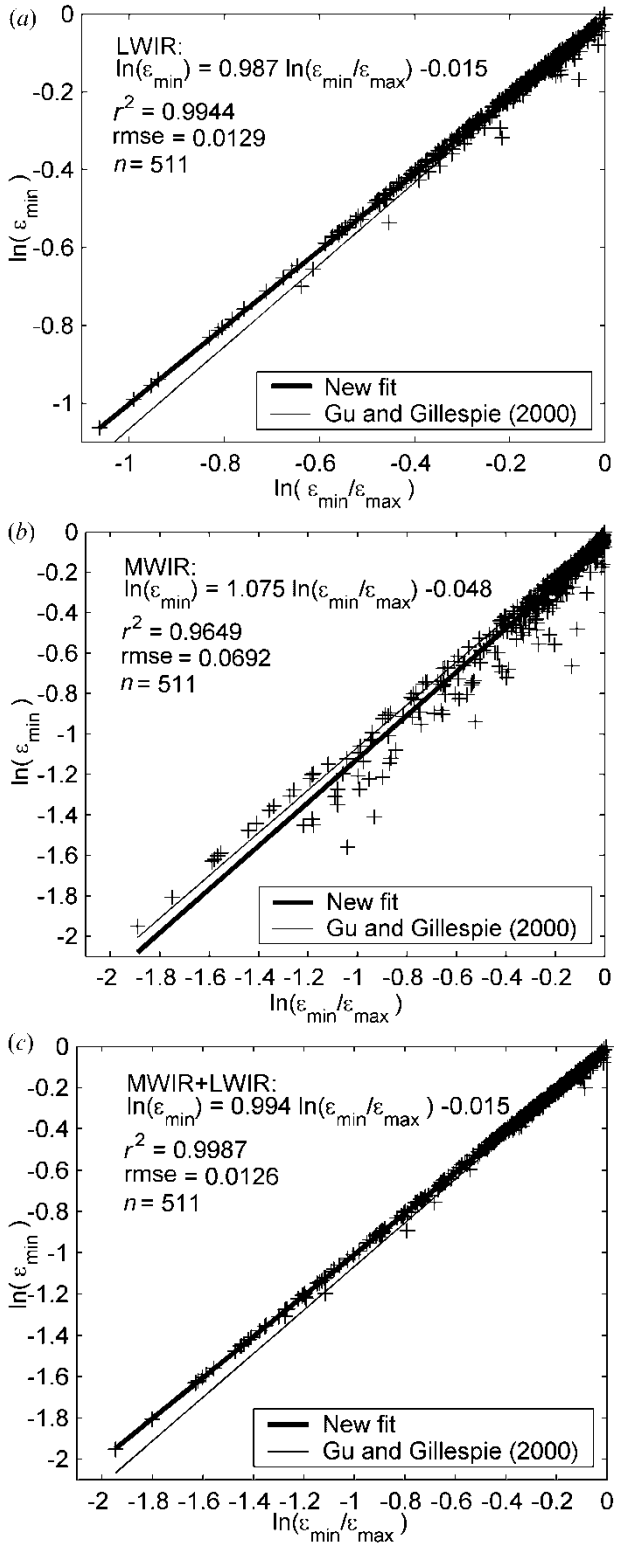
(a)
LWIR:
ln(ε_min) = 0.987 ln(ε_min/ε_max) -0.015
r² = 0.9944
rmse = 0.0129
n = 511
New fit
Gu and Gillespie (2000)
ln(ε_min)
ln(ε_min/ε_max)
(b)
MWIR:
ln(ε_min) = 1.075 ln(ε_min/ε_max) -0.048
r² = 0.9649
rmse = 0.0692
n = 511
New fit
Gu and Gillespie (2000)
ln(ε_min)
ln(ε_min/ε_max)
(c)
MWIR+LWIR:
ln(ε_min) = 0.994 ln(ε_min/ε_max) -0.015
r² = 0.9987
rmse = 0.0126
n = 511
New fit
Gu and Gillespie (2000)
ln(ε_min)
ln(ε_min/ε_max)

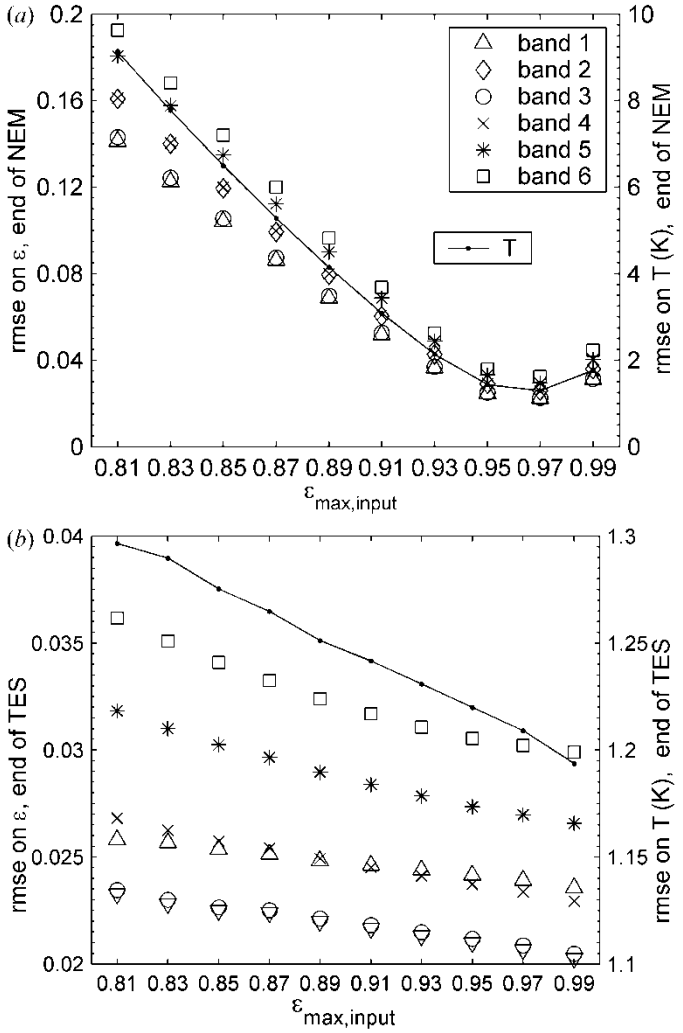


Figure 6. Rms error $\left(\text{rmse} = \frac{1}{\sqrt{n}}\sqrt{\sum_{surf=1}^{n}\left(\varepsilon_{j,surf}^{TRUE} - \varepsilon_{j,surf}^{NEM}\right)^2}\right)$ on emissivity calculated for each band (left axis) and on temperature (right axis) on 521 surfaces, (*a*) after NEM and (*b*) after TES.

surfaces have an $\varepsilon_{\max}$ around 0.97, it can be shown that the global error is minimum for $\varepsilon_{\max,\,input} = 0.97$ as seen in figure 6(*a*). Meanwhile the TES algorithm refines the emissivity minimum and is far less dependent than NEM to $\varepsilon_{\max,\,input}$ as seen on figure 6(*b*).

3.2.1.2. *Sensitivity of TES to empirical relationships*

Recalculated empirical MMD and MMR relationships were compared to the original relations presented by Gillespie *et al.* (1998) and by Gu and Gillespie (2000). We found that the original MMD relation allows for the best estimations of emissivities and temperature using the TES algorithm, as presented in table 1.

Table 1. Rmse after TES on emissivity and temperature for all 521 surfaces used for simulation for different empirical relationships:
- MMD (original): $\varepsilon_{min} = 0.994 - 0.687\ MMD^{0.737}$;
- MMD (recalculated): $\varepsilon_{min} = 0.987 - 0.689\ MMD^{0.749}$;
- MMR (original): $\ln(\varepsilon_{min}) = 1.056 \ln(\varepsilon_{min}/\varepsilon_{max}) - 0.01$;
- MMR (recalculated): $\ln(\varepsilon_{min}) = 1.046 \ln(\varepsilon_{min}/\varepsilon_{max}) - 0.034$;
- MMD (ratio with $\varepsilon_{8-14}$): $\varepsilon_{min} = 0.982 - 0.741\ MMD_{8-14}^{0.810}$,

to compute $MMD_{8-14}$ the broadband emissivity corresponding to CIMEL band 1 is used to ratio each NEM emissivity in equation (9).

| $n = 521$ | MMD (origin.) | MMD (recalc.) | MMR (origin.) | MMR (recalc.) | MMD (ratio with $\varepsilon_{8-14}$) |
|---|---|---|---|---|---|
| Band 1 | 0.024 | 0.024 | 0.031 | 0.024 | 0.024 |
| Band 2 | 0.021 | 0.021 | 0.027 | 0.021 | 0.021 |
| Band 3 | 0.021 | 0.021 | 0.027 | 0.021 | 0.021 |
| Band 4 | 0.023 | 0.024 | 0.031 | 0.025 | 0.024 |
| Band 5 | 0.027 | 0.027 | 0.035 | 0.028 | 0.028 |
| Band 6 | 0.030 | 0.030 | 0.039 | 0.031 | 0.030 |
| $T$ (K) | 1.21 | 1.24 | 1.53 | 1.21 | 1.22 |

These results led us to choose a value of 0.97 for $\varepsilon_{max}$ as the set input parameter to the NEM module and to use the original MMD relation (equation (11)) for optimum estimations of emissivities and temperature using the TES algorithm. In these conditions, the rmse on estimated emissivities for the selected spectra from the ASTER spectral library range from 0.02 to 0.03 depending on the band considered, and rmse on estimated temperature is 1.2 K (table 1).

It is important to note that the accuracy of emissivity and temperature retrieval using the TES algorithm is strongly correlated to the degree to which the surface considered matches the MMD relationship. Figure 7 represents rmse on temperature and emissivity for each band, as a function of the distance between the surface true minimum emissivity and the MMD fit. As shown in figure 7, samples having a low $\varepsilon_{max}$ are generally characterized by large errors on the estimated temperature. Corresponding estimated emissivities are also less accurate.

Liang (2001) also made this statement while developing empirical relationships and proposed an equation for each range of $\varepsilon_{max}$, which supposes an *a priori* knowledge of the considered surface.

### 3.2.2. *TES sensitivity for hyperspectral simulations*

Simulations were carried out for three different spectral domains: LWIR, MWIR and MWIR + LWIR in order to confirm the applicability of TES in each case. The averaged error over all the surfaces for temperature and also over all the wavelengths for emissivity is presented in table 2.

With the spectral TES it is possible to recover the emissivity in LWIR with an rmse of 0.022 over the emissivity and of 0.3 over the temperature. However, in MWIR the algorithm does not work in the case of simulated measurements in the Sun (see table 2). This can be explained partly by the fact that in this spectral domain, the reflected portion of the environment radiation, i.e. $(1-\varepsilon_\lambda) \times \left(L_{atm\downarrow,\lambda} + E_{sun,\lambda}/\pi\right)$, is of the same order of magnitude as the signal emitted by the surface. A slight imprecision in the atmospheric correction of the signal will therefore have a strong influence on the emissivity spectrum recovered.

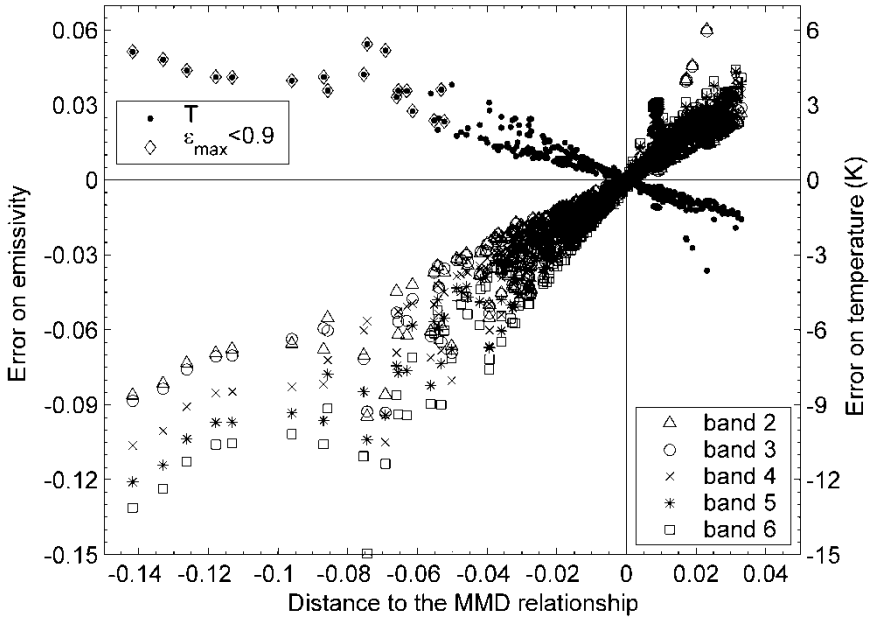


Figure 7. Error after TES for emissivity (left axis, $\varepsilon_{j,surf}^{TRUE} - \varepsilon_{j,surf}^{TES}$) and temperature (right axis, $T_{surf}^{TRUE} - T_{surf}^{TES}$) as a function of the distance of each surface emissivity from the MMD relationship, e.g. the difference between $\varepsilon_{\min}$ of the 'true' spectrum and $\varepsilon_{\min}$ estimated with MMD relationship (equation (10)). A diamond surrounding the temperature error symbol identifies surfaces with low $\varepsilon_{\min}$ (i.e. $<0.9$).

Table 2. Rmse on emissivity and temperature for hyperspectral data. Simulations procedures were run in three spectral regions: LWIR and MWIR, LWIR alone, MWIR alone.

| | LWIR + MWIR | | LWIR | | MWIR | |
|---|---|---|---|---|---|---|
| $n = 511$ | Sun | shade | Sun | shade | Sun | shade |
| Emissivity | 0.344 | 0.022 | 0.022 | 0.022 | 0.335 | 0.034 |
| $T$ (K) | 37.47 | 0.32 | 0.31 | 0.31 | 37.46 | 0.89 |

Also, we have shown in §3.1.2 that the empirical relationship MMR is not very accurate in the case of data in MWIR. For the emissivity spectra recovered with TES applied over the complete MWIR + LWIR spectral domain, the typical error of MWIR has repercussions over the entire spectrum. Nevertheless, it seems possible to recover correctly the emissivity in MWIR by carrying out measurements in the shade (e.g. with a screen hiding the Sun). If during the simulations we suppress solar illumination, the rmse values obtained are comparable to those obtained in LWIR (see table 2 and figure 8).

Finally, we found that the output error of TES is correlated with the degree to which the surface confirms the empirical relation MMR, as in the multiband case.

Results are encouraging with regard to the application of TES to hyperspectral data.

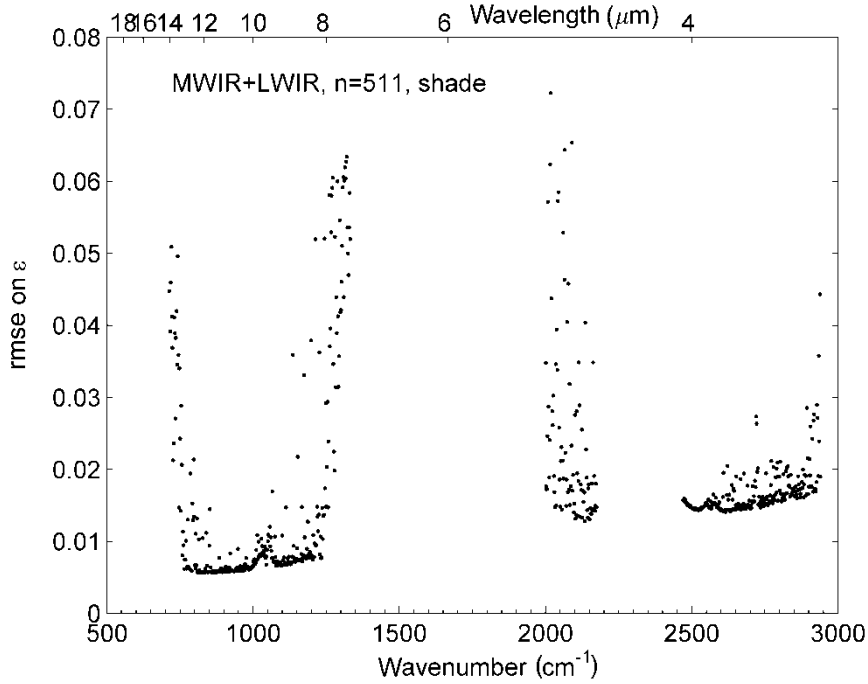


Figure 8. Error on emissivity after TES for hyperspectral simulations on LWIR and MWIR versus wavenumbers.

## 4. Adapted inversion methods

Three groups of surface types were identified from our analysis as being badly modelled by the TES algorithm. These are the surfaces characterized by high emissivity contrast (MMD $>0.6$), by a low $\varepsilon_{max}$ ($<0.9$) and metals.

We describe below improved inversion techniques to recover emissivities for these particular surfaces.

### 4.1. *Use of broadband emissivity to constrain high contrast*

We found that an MMR empirical equation improved the accuracy of emissivities and temperature retrieval for highly contrasted surfaces, decreasing rmse on emissivity from 0.04 to 0.01 for these surfaces (see table 3).

Table 3. Rmse calculated on emissivity and temperature after TES for surfaces with high contrast (i.e. MMD $>0.6$) for three empirical relationships: the original MMD and the recalculated MMR relationships, plus a modified MMD module (see table 1 caption for coefficients).

| $n=9$ | MMD (original) | MMR (recalculated) | MMD (ratio with $\varepsilon_{8-14}$) |
|---|---|---|---|
| Band 1 | 0.043 | 0.014 | 0.024 |
| Band 2 | 0.045 | 0.014 | 0.025 |
| Band 3 | 0.044 | 0.014 | 0.025 |
| Band 4 | 0.025 | 0.008 | 0.014 |
| Band 5 | 0.039 | 0.012 | 0.021 |
| Band 6 | 0.054 | 0.015 | 0.027 |
| $T$ (K) | 2.62 | 0.86 | 1.48 |

If a power law is still preferred, we propose to use broadband emissivity to ratio NEM emissivities in equation (9) instead of the average. Broadband emissivity is estimated from radiance measurements on band 1 of our radiometer (8–13.3 $\mu$m) using the temperature estimated by the NEM:

$$\varepsilon_{8-14} = \frac{L_{sens,1} - L_{atm\downarrow,1}}{B_1(T_{NEM}) - L_{atm\downarrow,1}} \tag{19}$$

As shown in table 3, the accuracy on retrieved emissivity using the MMD relation is enhanced by the use of broadband emissivity but the MMR relationship gives better results. It must be noted that these two methods can also be applied to all surfaces (see table 1), i.e. not only characterized by high emissivity contrast, allowing their use without *a priori* knowledge on surface types.

If the sensor considered has no broadband channel, the MMR relationship should be used, the broadband having the advantage of providing additional information, which is not the case if we try to recompute this broadband emissivity using a linear relationship between the other band emissivities for example.

Finally, it should be noted that the surface heterogeneity corresponding to a larger field of view (e.g. sensor on an aircraft or on a satellite) will certainly reduce spectral contrast, thus the problem will be less crucial.

### 4.2. *Surfaces with low maximum emissivity have to be treated separately*

The TES algorithm will also not properly recover spectra with low $\varepsilon_{\max}$. This comes from the fact that the NEM module assumes an $\varepsilon_{\max}$ of 0.97 and that these spectra do not satisfy the MMD relationships. Nevertheless, results can be significantly improved by using the NEM algorithm alone with an $\varepsilon_{\max}$ input of 0.87, assuming that these surfaces were previously identified. Table 4 compares errors after TES and NEM.

### 4.3. *Metals could be processed using the Sun–Shade Method in MWIR*

Finally, the TES algorithm fails to recover metal emissivity spectra. As the emissivity of metals is very low, all the methods assuming a high emissivity maximum are inappropriate. Nevertheless, MWIR reflectance of metals can be recovered by considering radiances measured alternatively while the sample is illuminated by the Sun and shaded from it. It is imperative that the temperature of

Table 4. Rmse on emissivity and temperature for multiband data only for surfaces with low maximum emissivity (i.e. $<0.9$). The first column concerns data processed with TES with an $\varepsilon_{\max}^{input}$ of 0.97 and the second column concerns data processed with NEM only, with an $\varepsilon_{\max}^{input}$ of 0.87.

| $n=18$ | TES, $\varepsilon_{\max}^{input}=0.97$ | NEM, $\varepsilon_{\max}^{input}=0.87$ |
|---|---|---|
| Band 1 | 0.078 | 0.015 |
| Band 2 | 0.067 | 0.013 |
| Band 3 | 0.068 | 0.013 |
| Band 4 | 0.075 | 0.015 |
| Band 5 | 0.088 | 0.018 |
| Band 6 | 0.103 | 0.020 |
| $T$ (K) | 4.02 | 0.85 |

the sample remains constant between both measurements. By comparison to measurements on a standard diffuse reflectance plate, the sample reflectance is then evaluated by:

$$\rho_{sample} = \rho_{stdRefl} \frac{L^{sun}_{sample} - L^{shade}_{sample}}{L^{sun}_{stdRefl} - L^{shade}_{stdRefl}} \tag{20}$$

This method was proposed as the Sun–Shade Method by Malaplate (2001) and can be applicable on diffuse metal surfaces. Specular surfaces remain a problem.

## 5. Examples of experimental results

We present here a few examples of experimental measurements carried out using the radiometer and the spectroradiometer previously mentioned. The data were processed using TES adapted to each data type.

### 5.1. *Experimental design*

We used a six-band radiometer developed by CIMEL Electronique, France (model CE 312-2). A technical description of a similar prototype using four bands can be found in Sicard *et al.* (1999) and Legrand *et al.* (2000). It is a portable field instrument designed to measure radiances of a remote target with a 10° field of view. The sensor is a thermopile and the spectral channels (figure 3) are selected with a filter wheel. It uses its internal radiance to compute the target effective radiance. A control unit distinct from the optical head allows automated acquisitions. During our measurements, targets were observed from a height of 30 cm with a 20° incidence angle, corresponding to a footprint of about 13 cm in diameter.

The second instrument is a FTIR emission spectroradiometer (a modified BOMEM MB100). It has a horizontal field of view of 40 mrad; a thermal mirror was placed at 45° in front of the aperture in order to look downward. It has two liquid nitrogen cooled quantum detectors: an indium antimonide (InSb) detector for the MWIR region and a mercury cadmium telluride (MTC) detector for the LWIR region. This spectroradiometer allows spectra acquisition between 500 and 5000 $cm^{-1}$ (2–20 $\mu$m) at a finest resolution of 1 $cm^{-1}$. The final radiance spectrum considered results from automatically co-adding 30 scans acquired with a spectral resolution of 4 $cm^{-1}$. The calibration procedures, as suggested by Revercomb *et al.* (1988), use a Mikron blackbody as reference at two different temperatures (15°C and 50°C), from a 30 cm optical path. The other samples were placed at an 80 cm optical path, which corresponds to a footprint of about 3.5 cm in diameter.

For both instruments, the measurements were carried out outdoors in clear sky conditions, at different dates in summer. The measurements on the samples were made alternatively with measurements on a diffuse reflectance standard plate (Infragold from Labsphere Inc.) to estimate the environment contribution ($L_{env,\lambda}$ or $L_{env,j}$). The samples considered were SiC and $SiO_2$ powders of known grain size (SiC: 14 $\mu$m, 45 $\mu$m, 120 $\mu$m; and $SiO_2$: 65 $\mu$m, 300–400 $\mu$m) at ambient temperature. We chose $SiO_2$ (or quartz) because it is a common constituent of Earth's surface (sand and soil) and it has a characteristic LWIR signature. We chose SiC for its characteristic signature in the 8–14 $\mu$m region with a strong absorption near 12 $\mu$m although it is not a natural material.

5.2. *Discussion on the measurements*

Figure 9(*a*) illustrates band emissivities for $SiO_2$ powders of different grain sizes. We compare emissivities retrieved with TES from radiance measurements acquired with the CIMEL 312-2 radiometer and band emissivity values integrated from $SiO_2$ JPL library spectra. The shape of the $SiO_2$ spectra is in agreement with what is found in the literature (see also quartz spectra in Korb *et al*. 1999 and ASTER band emissivities of a quartzite soil—e.g. sample 0135—in Salisbury and D'Aria 1992). We found a minimum at the band centred at 9.14 $\mu$m and two weak values for the 8.43 $\mu$m and the 8.68 $\mu$m bands corresponding to silicate restrahlen bands (strong absorption at 8 and 9 $\mu$m due to asymmetric Si–O stretching vibration).

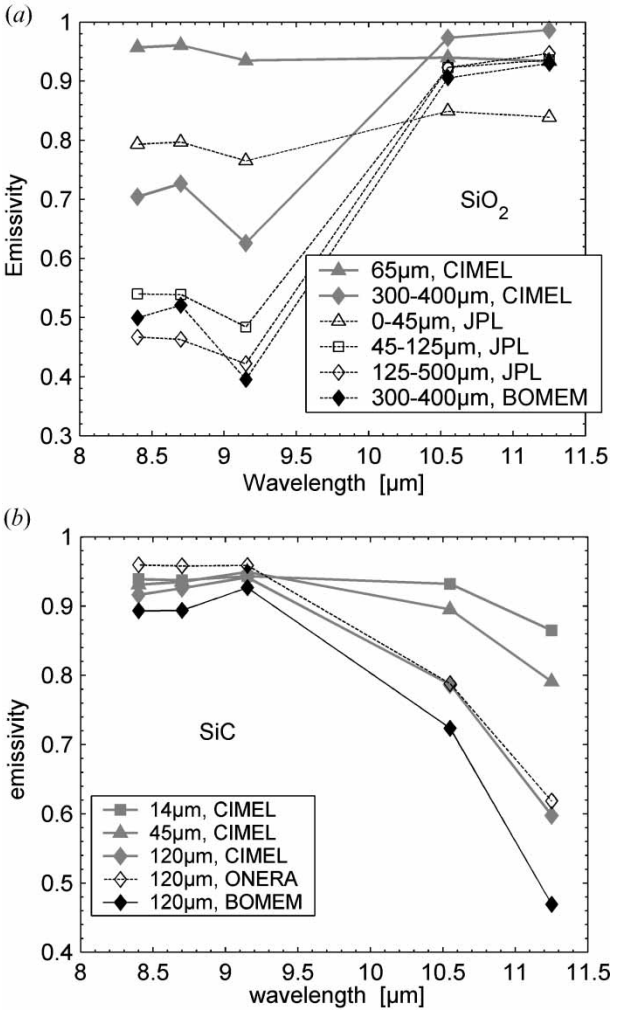


Figure 9. Emissivities for $SiO_2$ (*a*) and SiC (*b*) powders of different sizes. CIMEL means that multiband emissivities are retrieved with TES from radiance measurements acquired with the CIMEL 312-2 radiometer. BOMEM means that band emissivities are calculated by integrating (equation (14)) emissivity spectra measured by the BOMEM FTIR spectroradiometer. Lines identified by JPL and ONERA are reference emissivities calculated by integrating emissivity spectra deduced from JPL library or ONERA reflectance spectra, using Kirchhoff's law.

Concerning the SiC powder, we show on figure 9(*b*) the CIMEL measurements and band emissivity values integrated from SiC reflectance spectrum measured by the Office National d'Etudes et de Recherches Aérospatiales (ONERA, Toulouse, France) laboratory with an integrating sphere (X. Briottet, personal communication, 2001). For the same grain size, the agreement between both datasets is satisfying.

We can observe on figure 9(*a*) and (*b*) a reduction in the contrast with decreasing grain size for the measurements and for the reference spectra, in agreement with analysis by Salisbury and Wald (1992).

Figure 10(*a*), (*b*) and (*c*) shows emissivity spectra retrieved using the TES algorithm from radiance measurements acquired with the BOMEM MB100 spectroradiometer on SiC (120 $\mu$m) and $SiO_2$ (300–400 $\mu$m) powders. We compared these spectra with those obtained with the Maximum Temperature Method described by Hook and Kahle (1996) and using equation (21) to retrieve the emissivity spectrum.

$$\varepsilon_\lambda = \frac{L_{sens,\lambda} - L_{env,\lambda}}{B_\lambda\left(T^*_{\max}\right) - L_{env,\lambda}} \tag{21}$$

with $T^*_{\max}$ the maximum radiative temperature. Spectra retrieved by the two methods are similar for measurements made on shaded surfaces (figure 10(*a*) and (*b*)) but not for measurements made on surfaces directly illuminated by the Sun (e.g. for SiC on figure 10(*c*)). The Maximum Temperature Method diverges when blackbody radiance and environment radiance are of the same order of magnitude, which is the case in MWIR where direct solar illumination is not negligible. Moreover, we plotted on figure 10(*a*) and (*b*) the reference spectra described above from JPL (pure $SiO_2$, 125–500 $\mu$m) and ONERA (SiC). We can see that the spectra have similar shapes with differences in amplitude.

In order to compare measurements obtained with our two instruments, we computed band emissivities from the measured spectra of SiC and $SiO_2$ in the shade using equation (14). These values are presented in figure 9 (identified as BOMEM in caption). The features are similar but we observe a larger magnitude in the spectra obtained with the spectroradiometer with regard to the values by band obtained with the radiometer for the same samples. The analysis of these differences needs further investigation; however, they could arise from an overestimation in the environmental radiance $(L_{env,\lambda})$ measurement. Such an overestimation could lead to a too important atmospheric correction in the NEM module, especially at strong spectral features (high reflectivity and low emissivity), leading to a decrease of the estimated sample radiance and consequently of the calculated emissivity.

Nevertheless, these measurements can be seen as a first validation of the applicability of the TES algorithm to hyperspectral data and further experiments are required on TES optimization for high spectral resolution data.

---

Figure 10. Emissivity spectra retrieved with TES (circles) from radiance measurements acquired with a BOMEM MB100 FTIR emission spectroradiometer on $SiO_2$ powder in the shade (*a*), on SiC powder in the shade (*b*) and on SiC powder in the Sun (*c*). Spectra estimated using the Maximum Temperature Method are represented with stars. We plotted in continuous line reference spectra deduced from JPL library or ONERA reflectance spectra, using Kirchhoff's law.

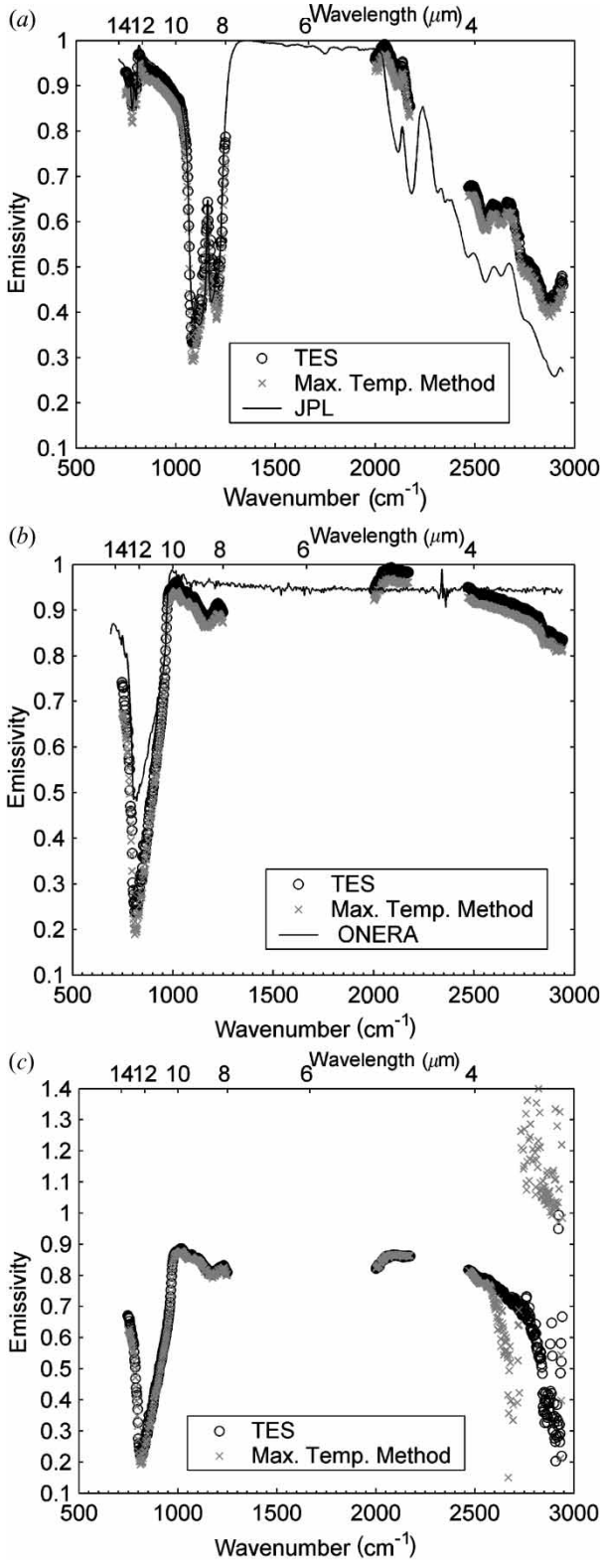
(a)
Wavelength (μm)
14 12 10 8 6 4
Emissivity
Wavenumber (cm-1)
TES
Max. Temp. Method
JPL
(b)
Wavelength (μm)
14 12 10 8 6 4
Emissivity
Wavenumber (cm-1)
TES
Max. Temp. Method
ONERA
(c)
Wavelength (μm)
14 12 10 8 6 4
Emissivity
Wavenumber (cm-1)
TES
Max. Temp. Method

## 6. Conclusion

This paper proposes some refinements to TES and confirms its performance. We investigated TES accuracy with numerical simulations using the ASTER spectral library and the MODTRAN code, in order to validate its applicability for ground measurements and for a large range of surfaces. The original MMD relationship gives the best results for multispectral data, and TES allows emissivity retrieval within 0.03 and temperature within 1.2 K.

We assessed TES applicability to hyperspectral data with an MMR empirical relationship in LWIR and in MWIR for shaded surfaces, but we showed that emissivity estimation from MWIR measurements when the Sun directly illuminates surfaces is not possible with this algorithm. Simulations show that spectral emissivity can be retrieved within 0.022 and temperature within 0.3 K in LWIR. Preliminary measurements acquired with a FTIR spectroradiometer are encouraging.

Moreover, we stated that metal emissivity cannot be recovered with this type of algorithm. High contrast surfaces are better processed with recalculated relationships also applicable to other types of surfaces. Low $\varepsilon_{max}$ samples need an adapted algorithm but are hardly identifiable without *a priori* knowledge.

These results clearly show that, for most natural surfaces, ground-based LWIR measurements alternated over a target and a diffuse reflective panel (such as Infragold) allow estimating emissivity and accurate surface temperature of this target without any assumption using the iterative TES algorithm. This approach can be simply applied in the field with a portable radiometer connected to a laptop for real time processing.

## Acknowledgments

This work was co-funded by the Natural Sciences and Engineering Council of Canada (NSERC), FQRNT–Action Concertée Québec and Defence R&D Canada–Valcartier (DRDC–Valcartier), who also provided the BOMEM MB 100 FTIR spectroradiometer. The authors would specially like to thank Jean-Marc Thériault at DRDC–Valcartier for his support concerning hyperspectral measurements and MB 100 data processing. We would also like to thank Frédéric Chagnon for the CIMEL radiometer measurements. We are also grateful to Françoise Nerry for helpful comments.

## References

BECKER, F., and LI, Z. L., 1990, Temperature-independent spectral indices in thermal infrared bands. *Remote Sensing of Environment*, **32**, 17–33.

BECKER, F., and LI, Z. L., 1995, Surface temperature and emissivity at various scales: definition, measurement and related problems. *Remote Sensing Reviews*, **12**, 225–253.

DASH, P., GÖTTSCHE, F.-M., OLESEN, F.-S., and FISCHER, H., 2002, Land surface temperature and emissivity estimation from passive sensor data: theory and practice—current trends. *International Journal of Remote Sensing*, **23**, 2563–2594.

GILLESPIE, A. R., ROKUGAWA, S., MATSUNAGA, T., COTHERN, J. S., HOOK, S., and KAHLE, A. B., 1998, A Temperature and Emissivity Separation algorithm for Advanced Spaceborne Thermal Emission and Reflection radiometer ASTER images. *IEEE Transactions on Geoscience and Remote Sensing*, **36**, 1113–1126.

GU, D., and GILLESPIE, A. R., 2000, A new approach for temperature and emissivity separation. *International Journal of Remote Sensing*, **21**, 2127–2132.

HOOK, S., GABEL, A. R., GREEN, A. A., and KEALY, P. S., 1992, A comparison of techniques for extracting emissivity information from thermal infrared data for geologic studies. *Remote Sensing of Environment*, **42**, 123–135.

HOOK, S., and KAHLE, A. B., 1996, The Micro Fourier Transform Interferometer ($\mu$FTIR)—A

new field spectroradiometer for acquisition of infrared data of natural surfaces. *Remote Sensing of Environment*, **56**, 172–181.

KORB, A. R., SALISBURY, J. W., and D'ARIA, D. M., 1999, Thermal-infrared remote sensing and Kirchhoff's law: 2. Field measurements. *Journal of Geophysical Research*, **104**, 15 339–15 350.

LEGRAND, M., PIETRAS, C., BROGNIEZ, G., HAEFFELIN, M., ABUHASSAN, N. K., and SICARD, M., 2000, A high-accuracy multiwavelength radiometer for *in situ* measurements in the thermal infrared. Part 1: Characterization of the instrument. *Bulletin of the American Meteorological Society*, **17**, 1203–1214.

LI, Z. L., BECKER, F., STOLL, M. P., and WAN, Z., 1999, Evaluation of six methods for extracting relative emissivity spectra from thermal infrared images. *Remote Sensing of Environment*, **69**, 197–214.

LIANG, S., 2001, An optimization algorithm for separating land surface temperature and emissivity from multispectral thermal infrared imagery. *IEEE Transactions on Geoscience and Remote Sensing*, **39**, 264–274.

MA, X. L., WAN, Z., MOELLER, C. C., MENZEL, W. P., GUMLEY, L. E., and ZHANG, Y., 2000, Retrieval of geophysical parameters from Moderate Resolution Imaging Spectroradiometer thermal infrared data: evaluation of a two-step physical algorithm. *Applied Optics*, **39**, 3537–3550.

MALAPLATE, A., 2001, Radiométrie infrarouge: développement et validation de méthodes utilisant la bande 3–5 $\mu$m pour la détermination des paramètres de surface à haute résolution spatiale. Thèse de doctorat, Université Louis Pasteur de Strasbourg I, Ecole Nationale Supérieure de Physique de Strasbourg, Strasbourg, France.

NICODEMUS, F. E., RICHMOND, J. C., and HSIA, J. J., 1977, Geometrical considerations and nomenclature for reflectance. Monograph 160, National Bureau of Standards, Washington, DC, USA, pp. 3–7.

NINOMIYA, Y., MATSUNAGA, T., YAMAGUCHI, Y., OGAWA, K., ROKUGAWA, S., UCHIDA, K., MURAOKA, H., and KAKU, M., 1997, A comparison of thermal infrared emissivity spectra measured *in situ*, in the laboratory, and derived from thermal infrared multispectral scanner TIMS data in Cuprite, Nevada, USA. *International Journal of Remote Sensing*, **18**, 1571–1581.

NORMAN, J. M., and BECKER, F., 1995, Terminology in thermal infrared remote sensing of natural surfaces. *Agricultural and Forest Meteorology*, **77**, 153–166.

OTTERMAN, J., SUSSKIND, J., BRAKKE, T., PIELKE, R., and LEE, T. J., 1994, Inferring the thermal-infrared hemispheric emission from a sparsely-vegetated surface by directional measurements. *Boundary-Layer Meteorology*, **74**, 163–180.

REVERCOMB, H. E., BUIJS, H., HOWELL, H. B., LAPORTE, D. D., SMITH, W. L., and SROMOVSKY, L. A., 1988, Radiometric calibration of IR Fourier transform spectrometers: solution to a problem with the High-Resolution Interferometer Sounder. *Applied Optics*, **27**, 3210–3218.

SALISBURY, J. W., and D'ARIA, D. M., 1992, Infrared (8–14 $\mu$m) remote sensing of soil particle size. *Remote Sensing of Environment*, **42**, 157–165.

SALISBURY, J. W., and WALD, A. E., 1992, The role of volume scattering in reducing spectral contrast of restrahlen bands in spectra of powered minerals. *Icarus*, **96**, 121–128.

SALISBURY, J. W., WALD, A. E., and D'ARIA, D. M., 1994, Thermal-infrared remote sensing and Kirchhoff's law: 1. Laboratory measurements. *Journal of Geophysical Research*, **99**, 11 897–11 911.

SICARD, M., SPYAK, P. R., BROGNIEZ, G., LEGRAND, M., ABUHASSAN, N. K., PIETRAS, C., and BUIS, J. P., 1999, Thermal infrared field radiometer for vicarious cross-calibration: characterization and comparisons with other field instruments. *Optical Engineering*, **38**, 345–356.

SOBRINO, J. A., LI, Z. L., STOLL, M. P., and BECKER, F., 1994, Improvements in the split-window technique for land surface temperature determination. *IEEE Transactions on Geoscience and Remote Sensing*, **32**, 243–253.

STAAF, Ö., RIBBING, C. G., and ANDERSSON, S. K., 1996, Temperature dependence of the band emittance for nongray bodies. *Applied Optics*, **35**, 6120–6125.

WAN, Z., and LI, Z. L., 1997, A physics-based algorithm for retrieving land-surface emissivity and temperature from EOS/MODIS data. *IEEE Transactions on Geoscience and Remote Sensing*, **35**, 980–996.

WATSON, K., 1992, Spectral ratio method for measuring emissivity. *Remote Sensing of Environment*, **42**, 113–116.

YAMAGUCHI, Y., KAHLE, A. B., TSU, H., KAWAKAMI, T., and PNIEL, M., 1998, Overview of Advanced Spaceborne Thermal Emission and Reflection radiometer (ASTER). *IEEE Transactions on Geoscience and Remote Sensing*, **36**, 1062–1071.